Mantle wedge oxidation due to sediment-infiltrated deserpentinisation

Padrón-Navarta, J.A.[1,2*], López Sánchez-Vizcaíno, V.[3], Manuel D. Menzel[4], María Teresa Gómez-Pugnaire[1,5], Garrido, C.J.[1]

[1]*Instituto Andaluz de Ciencias de la Tierra (IACT), CSIC–Universidad de Granada, Av. Palmeras 4, 18100 Armilla, Granada, Spain.*

[2]*Géosciences Montpellier, Université de Montpellier & CNRS, F-34095 Montpellier cedex 5, France.*

[3]*Dpto. de Geología (Unidad Asociada al IACT, CSIC–UGR), Universidad de Jaén, Escuela Politécnica Superior, 23700 Linares, Jaén, Spain.*

[4] *Institute of Tectonics and Geodynamics, RWTH Aachen University, Aachen, Germany.*

[5]*Departamento de Mineralogía y Petrología, Universidad de Granada, 18002 Granada, Spain*

**corresponding author (e-mail: alberto.padron@csic.es)*

2476 words/Summary (219 words)

The Earth's mantle is oxygen-breathing through the sink of oxidised tectonic plates at convergent margins[1,2]. Ocean floor serpentinisation increases the bulk oxidation state of iron relative to dry oceanic mantle and results in a variable intake of other redox-sensitive elements such as sulphur[2,3]. The reversibility of seafloor oxidation in subduction zones during high-pressure dehydration of serpentinite ("deserpentinisation") at subarc depths and the capacity of the resulting fluids to oxidise the mantle source of arc basalts are highly contested[4–15]. Thermodynamic modelling[8,10,15], experiments[6,12,14], and metaperidotite study in exhumed high-pressure terrains[4,15,16] result in differing estimates of the redox state of deserpentinisation fluids, ranging from low to highly oxidant. Here we show that although intrinsic deserpentinisation fluids are highly oxidant, the infiltration of small fractions of external fluids equilibrated with metasedimentary rocks strongly modulates their redox state and oxidation-reduction capacity explaining the observed discrepancies in their redox state. Infiltration of fluids equilibrated with graphite-bearing sediments reduces the oxidant, intrinsic deserpentinisation fluids to oxygen fugacities similar to those observed in most graphite-furnace experiments and natural metaperidotites. However, infiltration of CO_2-bearing fluids equilibrated with modern GLOSS generates sulphate-rich, highly oxidising deserpentinisation fluids. We show that such GLOSS-infiltrated deserpentinisation fluids can effectively oxidise the mantle wedge of cold to hot subduction zones potentially accounting for the presumed oxidised nature of the source of arc basalts.

Main (701 words)

Interaction of seawater with the oceanic lithosphere results in alteration of the oceanic crust and hydration of mantle peridotite to serpentinite. Serpentinisation substantially increases the amount of water and the ferric iron over total iron ratio ($Fe^{3+}/\Sigma Fe$)[1,2,13,17,18] (Fig.1a; 0.4–1.0 with a median and an average value of 0.60 and 0.58, n = 601) relative to that of the Depleted MORB Mantle (DMM, 0.015–0.04)[19] (Fig. 1a), placing serpentinite among the most oxidised rocks of the altered oceanic lithosphere. Seafloor serpentinisation furthermore increases the content of redox-sensitive, multivalent elements, particularly sulphur, whose abundance varies by up to three orders of magnitude relative to DMM (Fig. 1b), reflecting a large variability of oxygen fugacity (fO_2) and S intake processes.

Subduction of altered oceanic lithosphere triggers the high-pressure (high-P) dehydration of serpentinite at intermediate slab depths of subduction zones, a process usually referred to as deserpentinisation. Deserpentinisation is considered the main volatile source of arc magmatism and likely plays an important role in the recycling of redox-sensitive elements[8,10,11,13] and the genesis of ore deposits[20]. More controversial is the potential role of deserpentinisation aqueous fluids as oxidation agents of the mantle wedge source of arc magmatism, accounting for the more oxidised nature of arc basalts relative to MORBs[5–8,12,14]. While there is a consensus that water is mostly recycled back to the crust and atmosphere by deserpentinisation, the oxidation of seafloor serpentinites (Fig. 1a) is generally thought to be irreversible. While pure molecular species in aqueous fluids have a limited oxidising capacity[21], the redox capacity of deserpentinisation electrolytic fluids highly depends on their content in oxidised species bearing multivalent elements, particularly sulphur[8,22,23]. Sulphur species with a high oxidising capacity —such as sulphates— are thermodynamically predicted during deserpentinisation at fO_2 near or above the hematite–magnetite oxygen buffer[8]. Most deserpentinisation experiments, however, yield significantly lower fO_2[12,14]. Rare metaperidotite formed by high-P dehydration of subducted serpentinite, now exhumed in metamorphic paleo-subduction terranes —Cerro del Almirez (CdA) and Cima di Gagnone (CdG)— also records lower oxidising conditions than those predicted by thermodynamic models[4,15,24]. High-P serpentinite (metaserpentinite) and metaperidotite from CdA have a rather narrow range of $Fe^{3+}/\Sigma Fe$ ratio (0.60–0.64, first and third quartile, n=27 and 0.24–0.33, n = 21 respectively, Fig. 1a) and magnetite content (3–4 wt.%, n=19 vs. 0.3–1.1 wt.%, n=11, Supplementary Fig. 1), and the transition from metaserpentinite to metaperidotite results in a 40 % decrease of its redox budget (from 0.7 to 0.4 mol/kg, Methods and Supplementary Fig. 4 and Table 1). The trend of decreasing $Fe^{3+}/\Sigma Fe$ content from metaserpentinite to metaperidotite in CdA has been ascribed to deserpentinisation[16] suggesting the reversibility of seafloor serpentinisation oxidation during subduction (Fig. 1a), yet the ultimate cause for such reversal has not been provided . Alternatively, this trend is ascribed to different extents of oceanic serpentinisation of their protoliths[4,15,24], implying the irreversibility of seafloor oxidation serpentinisation during subduction (Fig. 1a). This interpretation is however at odds with numerous textural and geochemical evidence for the provenance of CdA and CdG

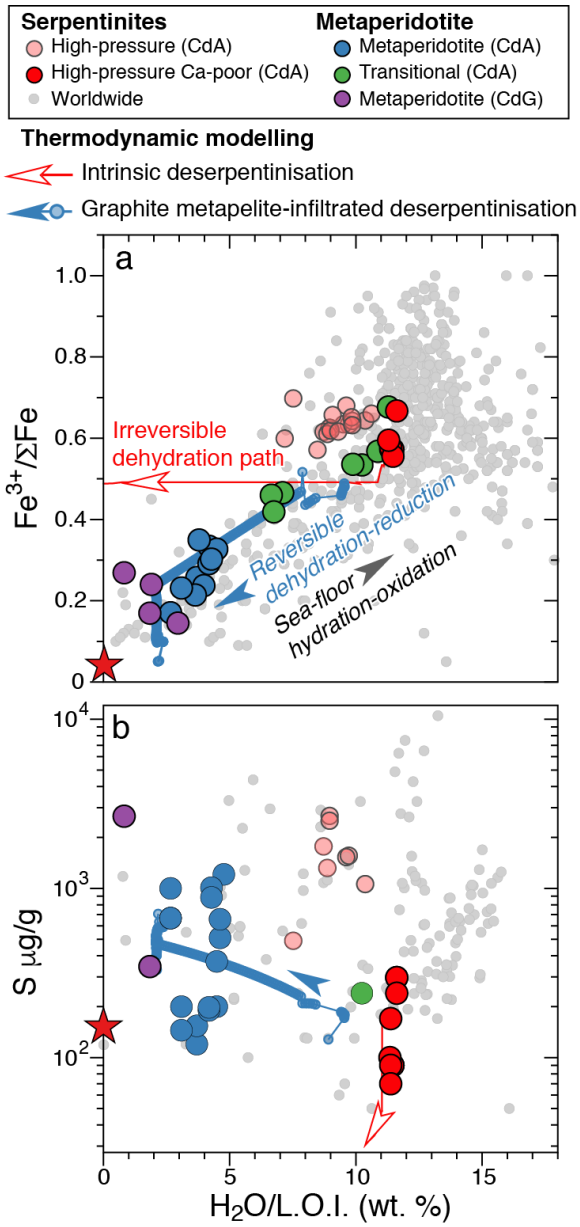

FIGURE 1a. The cycle of hydration-oxidation of mantle peridotite (serpentinites, grey arrow) at the Earth's ocean floor relative to the nominally anhydrous mantle (red star, Depleted MORB Mantle[9]) and two possible deserpentinisation paths either reversing or preserving the oxidation set at the Earth's surface. The directions of the arrows for the thermodynamically modelled intrinsic and graphite metapelite-infiltrated deserpentinisation evolutions indicate the direction of H_2O loss during subduction (depicted also in Fig. 2a). The only known rock samples from high-pressure terrains recording the deserpentinisation (metaperidotites from the Cerro del Almirez, CdA, and Cima di Gagnone, CdG, localities) match the reversible path requiring an external influx of reduced fluids during dehydration. Worldwide serpentinites also include partially serpentinized orogenic peridotites (< 9.0 wt.% H_2O, see Methods). **b.** The observed increase in total S content in the CdA and CdG metaperidotites compared to serpentinites is also reproduced by the graphite metapelite-infiltrated deserpentinisation model (blue arrow), in contrast to the intrinsic deserpentinisation model (red arrow).

metaperidotites from highly serpentinised peridotite protoliths metasomatised by crustal fluids[25–27]. CdA metaperidotite is also characterised by a moderate increase in S relative to its putative Ca-poor serpentinite protolith —with a low S content (< 300 μg/g) similar to DMM; an opposite trend to that predicted from thermodynamic modelling (Fig. 1b). Furthermore, subducted serpentinite has lower and narrower S contents than average oceanic serpentinite (Fig. 1b), thus limiting the capacity of deserpentinisation fluids to oxidise the mantle wedge. Thermodynamic modelling, experiments and natural samples thus provide seemingly contradictory views on the role of deserpentinisation fluids as potential agents for the oxidation of the mantle source of arc basalts.

The pervasiveness of subducted-sediment geochemical signatures is the hallmark of arc magmatism[28], an attribute increasingly ascribed to the interaction of slab crustal lithologies with slab fluids sourced from deserpentinisation. There is also overwhelming geochemical evidence on the role of infiltration of fluids equilibrated with metasedimentary rocks in the genesis of natural serpentinite-derived metaperidotite[25–27,29–33]. However, it has not yet been investigated how the interaction of sediment-derived fluids modify the fO_2 and the cargo of multivalent elements in the deserpentinisation fluids, compared to those sourced from the intrinsic (i.e. without external fluid infiltration) deserpentinisation.

Intrinsic deserpentinisation (396 words)

Figure 2a shows the thermodynamic modelling of the intrinsic prograde evolution a serpentinite subducted along the geothermal gradient of high-P metamorphic terrains. At constant bulk O_2 (red arrows in Fig. 1a and 2a, Supplementary Fig. 2), this evolution implies a dramatic increase of the $\Delta\log_{10}fO_2$[FMQ][7,10,34] from +2.2 (450 ºC, 0.9 GPa), where olivine is first produced, to +4.6 (660 ºC, 1.7 GPa), where antigorite serpentinite dehydrates to metaperidotite. The rise in fO_2 is due to the formation of hematite after magnetite to maintain the bulk $Fe^{3+}/\Sigma Fe$ constant (Fig. 1a; red line) since the X_{Mg} [Mg/(Fe^{2+}+Mg)] of olivine and orthopyroxene reaction products is lower than that of reactant antigorite (Supplementary Fig. 3 and 4). In agreement with previous models for a similar $\Delta\log_{10}fO_2$[FMQ][8], our model shows that S and C of serpentinite are fully dissolved in the deserpentinisation fluid , with $HSO_4^-{}_{(aq)}$ and, to a lesser extent, $SO_4^{2-}{}_{(aq)}$ as the dominant sulphur species (Supplementary Table 2).

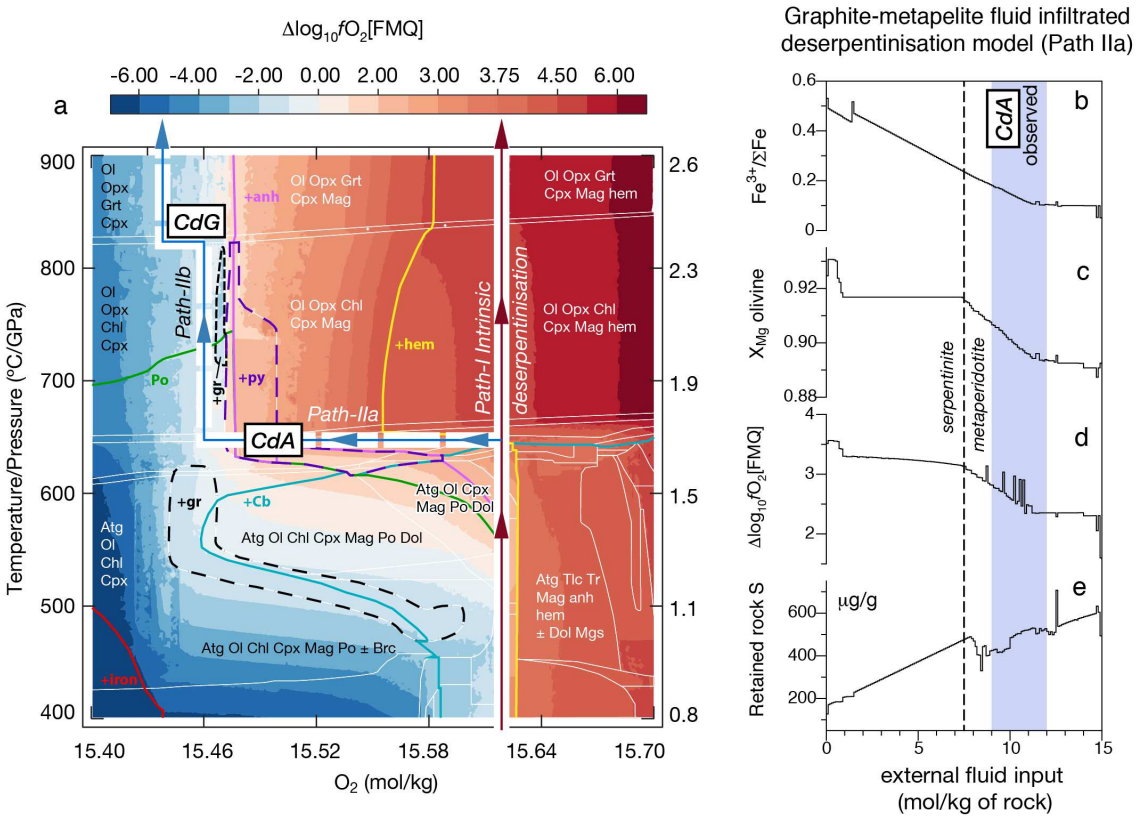

FIGURE 2a. Two potential evolutions of the oxygen fugacity fO_2 for the subducting serpentinite slab (expressed as relative to the FMQ buffer; see Methods) for a geothermal gradient crossing the antigorite (660 ºC/1.7 GPa) and chlorite dehydration (820 ºC/2.4 GPa) as observed at CdA and CdG computed for a representative fully serpentinized peridotite containing 5 wt.% magnetite, 11.6 wt.% H_2O, 170 ppm S, and 200 ppm C (Figure 1 and Supplementary Table 1). Stability fields highlighting some key mineral assemblages are superimposed as thick lines (see Supplementary Figure 2). Path-I ("Intrinsic deserpentinisation") corresponds to the conventional, closed system, prograde metamorphism where the rock imposes the fO_2 and shows a dramatic increase in the $\Delta\log_{10}fO_2$[FMQ] of up to +4.5. Here we show that, alternatively, externally-derived fluid infiltration can induce complete antigorite dehydration at isobaric-isothermal conditions (horizontal Path-IIa, graphite-metapelite infiltrated deserpentinisation) with a decrease in the relative fO_2 and in the redox budget if the infiltrating fluid is derived from a sediment (pyrite and graphite-bearing metapelite) with a high reducing capacity[46]. **b-e.** Isothermal and isobaric evolution (650 ºC/1.7 GPa) along the computed, dehydration-driven infiltration path. The vertical dashed line marks the complete deserpentinization (for the Path-I intrinsic evolution see Supplementary Figure 4): **b.** Bulk-rock ferric to total iron content ($Fe^{3+}/\Sigma Fe$). **c.** X_{Mg} in olivine. **d.** $\Delta\log_{10}fO_2$[FMQ]. **e.** Total sulphur content retained in the reacting rock during the external infiltration. The blue-shaded range shows the extent of fluid-rock reaction necessary to induce full dehydration of serpentinite and reproduce the observed $Fe^{3+}/\Sigma Fe$ and X_{Mg} in the CdA exhumed high-pressure terrain (metaperidotite).

103

The intrinsic deserpentinisation thermodynamic model fails to explain many features of natural serpentinite and metaperidotite, such as the decrease of the bulk $Fe^{3+}/\Sigma Fe$[4,16,35] and the relative increase in S content in metaperidotite[36] (Fig. 1); its magnetite content and lack of hematite[4,16,24,35] (Supplementary Fig. 1); and the lower olivine X_{Mg}[4,35] (Supplementary Fig. 4). Nor does it explain the substantially lower $\Delta\log_{10}fO_2$[FMQ] (+2.1 ± 0.3; at 800 ºC, 1GPa) found in most high-P serpentinite dehydration experiments[12,14,37–39] that obtain olivine —coexisting with magnetite[6,14,40]— with an X_{Mg} that perfectly matches that of natural metaperidotite[4,15,35,41]. Although these lines of evidence might point to the non-validity of the thermodynamic model of intrinsic deserpentinisation, it is well known that the fO_2 is externally buffered and biased towards lower fO_2 in high-T, long-run, graphite-furnace experiments[14]. Interestingly, deserpentinisation experiments conceived to maintain high fO_2 using $LaCrO_3$ instead of graphite furnace[6] obtain high X_{Mg} olivine (0.94–0.97) coexisting with hematite and magnetite, and $\Delta\log_{10}fO_2$[FMQ] ranging from +3.1 to +4.1, in excellent agreement with our thermodynamic model predictions (Fig. 2 and Supplementary Fig. 4). As serendipitously attained in graphite-furnace experiments[12,14,37–39], many natural metaperidotite features would be matched if the bulk O_2 of the system was open, externally imposed and shifted towards lower bulk O_2 values (blue lines for CdA and CdG, respectively in Fig. 2a). This hypothesis would reconcile the seemingly contradictory fO_2 stemming from thermodynamic modelling, some experiments, and natural samples.

Sediment-fluid infiltration driven by deserpentinisation (553 words)

The infiltration of fluids equilibrated with metasedimentary rocks —well documented in the genesis of natural metaperidotite[25,33,42,43]—is a potential mechanism for modifying the fO_2 and multivalent element cargo of deserpentinisation fluids. Lowering the fO_2 relative to the oxidising conditions of intrinsic deserpentinisation (Fig. 2a) requires the infiltration of fluids in equilibrium with metasedimentary rocks with a highly reducing capacity, such as graphite-bearing sediments[44,45]. Graphite-bearing sediments and calc-silicates subducted to eclogite facies conditions during the Alpine orogeny are widely associated with the few known natural occurrences of metaperidotite derived from high-P deserpentinisation[33,46–48]. Figures 2b–e show the results of thermodynamic modelling of the infiltration of fluids equilibrated with graphite-bearing metapelite at a temperature 10 ºC colder than the intrinsic deserpentinisation conditions in the CdA (650 ºC, 1.7 GPa). At these conditions, serpentinite releases 2 wt.% of H_2O and generates sufficient permeability for external fluid infiltration. The metapelite-derived infiltrating aqueous fluid is rich in CH_4 and H_2S with minor H_2 (Supplementary Table 2). At the onset of its infiltration into dehydrating serpentinite, CH_4 is oxidised to CO_2, and the H_2S and H_2 concentrations decrease at the expense of more oxidised $HSO_4^-{}_{(aq)}$ and $SO_4^{2-}{}_{(aq)}$ species that increase compared to those in the intrinsic deserpentinisation fluid (Supplementary Table 2 and Fig. 5a). Sediment-fluid infiltration gradually decreases the bulk $Fe^{3+}/\Sigma Fe$ (Fig. 2b), thus decreasing its bulk rock and olivine X_{Mg} (Fig. 2c) due to a lower fO_2 (Fig. 2d), and increases the bulk S content of metaperidotite

and fluid (Fig. 2e and Supplementary Fig. 5a and Table 2). Complete dehydration occurs at isobaric and isothermal conditions with an infiltration as low as 7.4 mol/kg of a fluid equilibrated with a graphite-bearing metapelite (vertical dashed line in Fig. 2b-e).

For an infiltration extent of 9–12 mol/kg (ca. 0.2 fluid/rock mass ratio, Fig. 2b–e), sediment-equilibrated fluid infiltration driven by deserpentinisation fully succeeds in explaining many features of natural CdA serpentinite and metaperidotite, such as the trend of decreasing bulk $Fe^{3+}/\Sigma Fe$ (Fig. 1a; 0.17–0.10 in Fig.2b), the relative increase in metaperidotite bulk S content (ca. 400–500 μg/g S, Fig. 1b and 2e) relative to its metaserpentinite protolith (c. 170 μg/g), and the modal magnetite content (Supplementary Fig. 1) and lack of hematite in metaperidotite. It also predicts an olivine X_{Mg} (0.91–0.89, Fig. 2c) and $\Delta\log_{10}fO_2$[FMQ] (+2.7 to +2.3, Fig. 2d), in excellent agreement with the olivine X_{Mg} of CdA metaperidotite[4,15,35] and the fO_2 and olivine X_{Mg} obtained in graphite-furnace serpentinite dehydration experiments[12]. Compared to the intrinsic deserpentinisation, the infiltration of 9–12 mol/kg of sediment-equilibrated fluids does not significantly modify the bulk major element contents, silicate mineral assemblage or modal proportions of metaperidotite. This petrological similarity likely explains why sediment-fluid infiltration has only been considered responsible for the cryptic geochemical signature of natural metaperidotite but largely passed unnoticed as a mechanism to modulate the redox state and cargo of redox-sensitive elements during deserpentinisation. For an external fluid infiltration of > 11 mol/kg, the rise of H_2S and $HS^-_{(aq)}$ in the fluid results in pyrite precipitation (Supplementary Fig. 5b) —occasionally found in CdA metaperidotites— while maintaining an elevated concentration of $HSO_4^-{}_{(aq)}$, accounting for the observed increase of the $SO_4/\Sigma S$ ratio allied to a decrease in total $\delta^{34}S$ in metaperidotite relative to its serpentinite protolith reported in CdA[36].

Implications for the redox state of the subarc mantle (607 words)

The interaction of slab fluids with the subarc mantle wedge source is increasingly recognised [40,41] as the cause of the more oxidised nature of arc basalts relative to MORBs. Deserpentinisation is the main source of slab fluids at subarc depths and thus a possible mantle wedge oxidation agent. While the extent of serpentinisation of fast-spreading mid-ocean lithosphere is largely unconstrained, serpentinite is widespread in subducted slow-spreading, mid-ocean ridge lithosphere and at the slab interface of subduction zones. At the slab interface of hot to cold subduction zones, modelling shows that serpentinite intrinsically dehydrates between 2.4–3.4 GPa and 650–660 ºC under relatively oxidising conditions (+2.9 to +3.7 $\Delta\log_{10}fO_2$[FMQ]), particularly in hot subduction zones (see ID in Fig. 3a) due to the negative pressure dependence of $\Delta\log_{10}fO_2$[FMQ] for metaperidotites (Supplementary Fig. 6). The dominant fluid sulfur species in all thermal regimes is $HSO^{4-}_{(aq)}$, which is slightly more abundant in deserpentinisation fluids from —relatively more oxidant— hot subduction zones (Fig. 3a). At the slab interface, serpentinite coexists with fluid-saturated metasedimentary rocks in

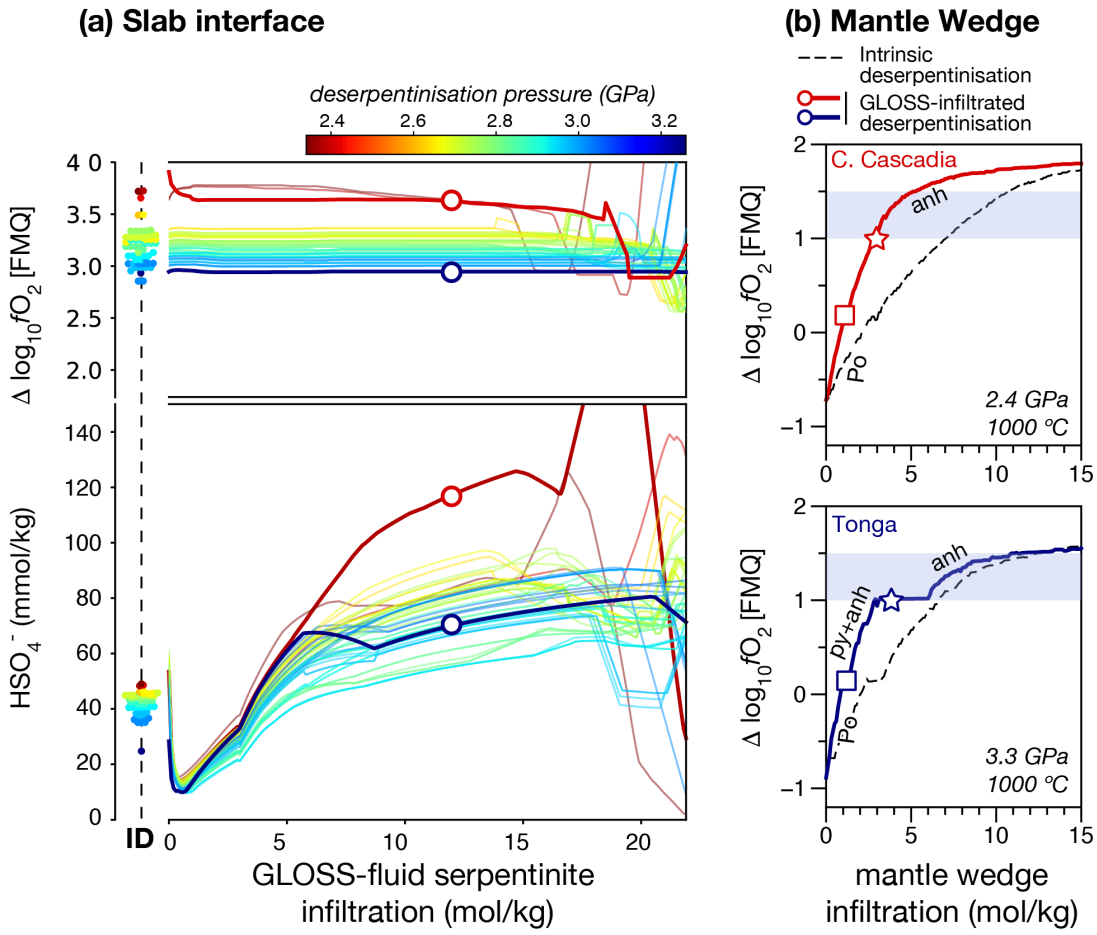

FIGURE 3a. Modification of the $\Delta\log_{10}fO_2$[FMQ] and the concentration of the main oxidising fluid species (HSO_4^-) relative to the intrinsic dehydration (ID) serpentinite fluid when serpentinites are infiltrated by sediment-derived fluids with low reducing capacity (GLOSS) for a worldwide compilation of subduction zones (color-coded for the pressure at which the serpentinite dehydrates at the slab surface, Methods). **b.** The capacity of these modified, serpentinite-derived fluids (empty dots in a) to oxidise the mantle wedge on top of the slab at near wet-solidus conditions is computed for the hottest (Central Cascadia) and coldest (Tonga) subduction zones. A minimum value range of $\Delta\log_{10}fO_2$[FMQ] inferred for oxidised IAB source and recorded by high-pressure metasomatized mantle atop of the slab[52,53] is given as a horizonal blue-shaded range. Sediment (GLOSS)-serpentinite derived fluids are more than two-fold more efficient (3 mol/kg) to oxidise the mantle wedge than the intrinsically-released serpentinite dehydration fluids (7 mol/kg). The metasomatized mantle wedge has an initial depleted composition. Squares and stars on the red and blue lines indicate the condition range limits at which pyrrhotite (Po), pyrite (py) or anhydrite (anh) are the stable minerals hosting S in the rocks. For an ultradepleted MORB mantle see Supplementary, Fig. 7. For an interaction with sediments with high reducing capacity (blackshale-like sediments) see Supplementary Fig. 8.

175

melange zones[49] and sediment-fluid infiltration driven by deserpentinisation is favoured. Modelling shows that for an extent of infiltration of 12 mol/kg —similar to that inferred from natural CdA (Fig. 2b-e)— infiltration of fluids equilibrated with modern Global Subducting Sediments (GLOSS)[21,42] during deserpentinisation does not greatly modify their fO_2 relative to intrinsic deserpentinisation whatever the subduction thermal regime (Fig. 3a). However, the abundance of dominant sulphate fluid species $HSO_4^-{}_{(aq)}$ increases notably in warm and hot subduction zones (Fig. 3a), boosting the redox capacity of deserpentinisation slab fluids relative to those produced by intrinsic dehydration.

Figure 3b shows the modelling of the fO_2 evolution of a DMM mantle wedge —at the near-vapour-saturated solidus temperature[50]— infiltrated by deserpentinisation fluids for a hot (Central Cascadia) and cold (Tonga) subduction zone. Infiltration of at least 7 mol/kg of slab fluids produced by intrinsic deserpentinisation is required to oxidise the mantle wedge within the minimum range of $\Delta\log_{10}fO_2$[FMQ] inferred for the mantle source of arc magmas (FMQ +1.0[51,52]). In contrast, GLOSS-infiltrated deserpentinisation fluids have a greater oxidising capacity; the interaction of about 3 mol/kg of these slab fluids drastically increases the $\Delta\log_{10}fO_2$[FMQ] of the mantle wedge in hot and cold subduction zones (Fig. 3b). Therefore the effectiveness of rock deserpentinisation required to oxidise the mantle wedge is increased by a factor of more than two compared to intrinsic deserpentinisation. In both thermal regimes, slab fluids can attain the inferred fO_2 of the mantle source of arc magmas by precipitating anhydrite, thought to be the main sulfur host at these fO_2 mantle wedge conditions[51]. Our results demonstrate that metasomatism of the mantle wedge with GLOSS-infiltrated deserpentinisation fluids is a viable mechanism to account for the oxidised nature of the mantle source of arc magmas in hot and cold subduction zones. Similar conclusions are obtained when considering a more depleted and reduced —due to dependence of the fO_2 on the peridotite bulk composition[53]— mantle wedge (Supplementary Fig. 7), indicating that the extent of mantle wedge depletion has a subsidiary role compared to the redox capacity of the incoming slab fluids.

As attested by natural metaperidotite, the oxidising capacity of sediment-infiltrated deserpentinisation fluids depends on the redox capacity of subducted sediments. This capacity has changed throughout Earth's geological history linked to the oxidation state of the atmosphere–ocean system and varies from oxidant GLOSS[28,54] to highly reducing black shales[44,45]. Modelling of deserpentinisation infiltrated by fluids equilibrated with graphite-bearing metapelite shows that in hot subduction zones the oxidant capacity of fluids is as high as for intrinsic deserpentinisation but is significantly lower for cold subduction zones (Supplementary Fig. 7 and 8).

References

1. Lécuyer, C. & Ricard, Y. Long-term fluxes and budget of ferric iron: Implication for the redox states of the Earth's mantle and atmosphere. *Earth Planet. Sci. Lett.* **165**, 197–211 (1999).
2. Evans, K. A. The redox budget of subduction zones. *Earth-Science Rev.* **113**, 11–32 (2012).

3. Alt, J. C. *et al.* The role of serpentinites in cycling of carbon and sulfur: Seafloor serpentinization and subduction metamorphism. *Lithos* **178**, 40–54 (2013).
4. Bretscher, A., Hermann, J. & Pettke, T. The influence of oceanic oxidation on serpentinite dehydration during subduction. *Earth Planet. Sci. Lett.* **499**, 173–184 (2018).
5. Debret, B. *et al.* Redox transfer at subduction zones: insights from Fe isotopes in the Mariana forearc. *Geochem. Persp. Let* **12**, 46–51 (2020).
6. Maurice, J. *et al.* The intrinsic nature of antigorite breakdown at 3 GPa: Experimental constraints on redox conditions of serpentinite dehydration in subduction zones. *Contrib. to Mineral. Petrol.* **175**, 94 (2020).
7. Evans, K. A. & Frost, B. R. Deserpentinization in Subduction Zones as a Source of Oxidation in Arcs: a Reality Check. *J. Petrol.* **62**, 1–32 (2021).
8. Debret, B. & Sverjensky, D. A. Highly oxidising fluids generated during serpentinite breakdown in subduction zones. *Sci. Rep.* **7**, 1–6 (2017).
9. Evans, K. A., Powell, R. & Holland, T. J. B. Internally consistent data for sulphur-bearing phases and application to the construction of pseudosections for mafic greenschist facies rocks in Na_2O–CaO–K_2O–FeO–MgO–Al_2O_3–SiO_2–CO_2–O–S–H_2O. *J. Metamorph. Geol.* **28**, 667–687 (2010).
10. Evans, K. A. & Powell, R. The effect of subduction on the sulphur, carbon and redox budget of lithospheric mantle. *J. Metamorph. Geol.* **33**, 649–670 (2015).
11. Evans, K. A., Reddy, S. M., Tomkins, A. G., Crossley, R. J. & Frost, B. R. Effects of geodynamic setting on the redox state of fluids released by subducted mantle lithosphere. *Lithos* **278**–**281**, 26–42 (2017).
12. Iacovino, K., Guild, M. R. & Till, C. B. Aqueous fluids are effective oxidizing agents of the mantle in subduction zones. *Contrib. to Mineral. Petrol. 2020 1754* **175**, 1–21 (2020).
13. Li, J. L. *et al.* Uncovering and quantifying the subduction zone sulfur cycle from the slab perspective. *Nat. Commun.* **11**, (2020).
14. Merkulova, M. V *et al.* Experimental insight into redox transfer by iron- and sulfur-bearing serpentinite dehydration in subduction zones. *Earth Planet. Sci. Lett.* **479**, 133–143 (2017).
15. Piccoli, F. *et al.* Subducting serpentinites release reduced, not oxidized, aqueous fluids. *Sci. Rep.* **9**, 19573 (2019).
16. Debret, B. *et al.* Redox state of iron during high-pressure serpentinite dehydration. *Contrib. to Mineral. Petrol.* **169**, 1–18 (2015).
17. Mayhew, L. E. & Ellison, E. T. A synthesis and meta-analysis of the Fe chemistry of serpentinites and serpentine minerals. *Philos. Trans. R. Soc. A Math. Phys. Eng. Sci.* **378**, 20180420 (2020).
18. Andreani, M., Muñoz, M., Marcaillou, C. & Delacour, A. μXANES study of iron redox state in serpentine during oceanic serpentinization. *Lithos* **178**, 70–83 (2013).
19. O'Neill, H. S. C. *et al.* Ferric Iron in the Upper Mantle and In Transition Zone Assemblages: Implications for Relative Oxygen Fugacities in the Mantle. in 73–88 (American Geophysical Union (AGU), 2013). doi:10.1029/GM074p0073.
20. Richards, J. P. The oxidation state, and sulfur and Cu contents of arc magmas: Implications for metallogeny. *Lithos* vol. 233 27–45 (2014).

21. Frost, R. & Ballhaus, C. Comment on '"Constraints on the origin of the oxidation state of mantle overlying subduction zones: An example from Simcoe, Washington, USA"' by A. D. Brandon and D. S. Draper. *Geochim. Cosmochim. Acta* **62**, 329–331 (1998).
22. Rielli, A. *et al.* Evidence of sub-arc mantle oxidation by sulphur and carbon. *Lett. Geochemical Perspect. Lett. Geochem. Persp. Let* **3**, 124–132 (2017).
23. Colin, A. *et al.* In situ determination of sulfur speciation and partitioning in aqueous fluid-silicate melt systems. *Geochemical Perspect. Lett.* 31–35 (2020) doi:10.7185/geochemlet.2020.
24. Vieira Duarte, J. F., Piccoli, F., Pettke, T. & Hermann, J. Textural and geochemical evidence for magnetite production upon antigorite breakdown during subduction. *J. Petrol.* (2021) doi:10.1093/petrology/egab053.
25. Garrido, C. J. *et al.* Enrichment of HFSE in chlorite-harzburgite produced by high-pressure dehydration of antigorite-serpentinite: Implications for subduction magmatism. *Geochemistry Geophys. Geosystems* **6**, (2005).
26. Scambelluri, M., Pettke, T., Rampone, E., Godard, M. & Reusser, E. Petrology and Trace Element Budgets of High-pressure Peridotites Indicate Subduction Dehydration of Serpentinized Mantle (Cima di Gagnone, Central Alps, Switzerland). *J. Petrol.* **55**, 459–498 (2014).
27. Debret, B. *et al.* Iron and zinc stable isotope evidence for open-system high-pressure dehydration of antigorite serpentinite in subduction zones. *Geochim. Cosmochim. Acta* **296**, 210–225 (2021).
28. Plank, T. & Langmuir, C. H. Tracing trace elements from sediment input to volcanic output at subduction zones. *Nature* **362**, 739–743 (1993).
29. Scambelluri, M. *et al.* The fate of B, Cl and Li in the subducted oceanic mantle and in the antigorite breakdown fluids. *Earth Planet. Sci. Lett.* **222**, 217–234 (2004).
30. John, T., Scambelluri, M., Frische, M., Barnes, J. D. & Bach, W. Dehydration of subducting serpentinite: Implications for halogen mobility in subduction zones and the deep halogen cycle. *Earth Planet. Sci. Lett.* **308**, 65–76 (2011).
31. Kendrick, M. A., Scambelluri, M., Hermann, J. & Padrón-Navarta, J. A. Halogens and noble gases in serpentinites and secondary peridotites: Implications for seawater subduction and the origin of mantle neon. *Geochim. Cosmochim. Acta* **235**, 285–304 (2018).
32. Harvey, J. *et al.* 11B-rich fluids in subduction zones: The role of antigorite dehydration in subducting slabs and boron isotope heterogeneity in the mantle. *Chem. Geol.* **376**, 20–30 (2014).
33. Marchesi, C., Garrido, C. J., Padrón-Navarta, J. A., López Sánchez-Vizcaíno, V. & Gómez-Pugnaire, M. T. Element mobility from seafloor serpentinization to high-pressure dehydration of antigorite in subducted serpentinite: Insights from the Cerro del Almirez ultramafic massif (southern Spain). *Lithos* **178**, 128–142 (2013).
34. Lazar, C. Using Silica Activity to Model Redox-dependent Fluid Compositions in Serpentinites from 100 to 700 °c and from 1 to 20 kbar. *J. Petrol.* **61**, (2020).
35. Padrón-Navarta, J. A. *et al.* Metamorphic record of high-pressure dehydration of antigorite serpentinite to chlorite harzburgite in a subduction setting (Cerro del Almirez, Nevado-Filábride complex, Southern Spain). *J. Petrol.* **52**, 2047–2078 (2011).
36. Alt, J. C. *et al.* Recycling of water, carbon, and sulfur during subduction of serpentinites: A stable

isotope study of Cerro del Almirez, Spain. *Earth Planet. Sci. Lett.* **327**–**328**, 50–60 (2012).
37. Padrón-Navarta, J. A. *et al.* Tschermak's substitution in antigorite and consequences for phase relations and water liberation in high-grade serpentinites. *Lithos* **178**, 186–196 (2013).
38. Padrón-Navarta, J. A., Hermann, J., Garrido, C. J., López Sánchez-Vizcaíno, V. & Gómez-Pugnaire, M. T. An experimental investigation of antigorite dehydration in natural silica-enriched serpentinite. *Contrib. to Mineral. Petrol.* **159**, 25–42 (2010).
39. Bromiley, G. D. & Pawley, A. R. The stability of antigorite in the systems MgO-SiO_2-H_2O (MSH) and MgO-Al_2O_3-SiO_2-H_2O (MASH): The effects of Al3+ substitution on high-pressure stability. *Am. Mineral.* **88**, 99–108 (2003).
40. Truckenbrodt, J., Ziegenbein, D. & Johannes, W. Redox conditions in piston-cylinder apparatus: The different behavior of boron nitride and unfired pyrophyllite assemblies. *Am. Mineral.* **82**, 337–344 (1997).
41. Evans, B. W. & Trommsdorff, V. Petrogenesis of garnet lherzolite, Cima di Gagnone, Lepontine Alps. *Earth Planet. Sci. Lett.* **40**, 333–348 (1978).
42. Scambelluri, M., Pettke, T. & Cannaò, E. Fluid-related inclusions in Alpine high-pressure peridotite reveal trace element recycling during subduction-zone dehydration of serpentinized mantle (Cima di Gagnone, Swiss Alps). *Earth Planet. Sci. Lett.* **429**, 45–59 (2015).
43. Cannaò, E., Agostini, S., Scambelluri, M., Tonarini, S. & Godard, M. B, Sr and Pb isotope geochemistry of high-pressure Alpine metaperidotites monitors fluid-mediated element recycling during serpentinite dehydration in subduction mélange (Cima di Gagnone, Swiss Central Alps). *Geochim. Cosmochim. Acta* **163**, 80–100 (2015).
44. Galvez, M. E., Fischer, W. W., Jaccard, S. L. & Eglinton, T. I. Materials and pathways of the organic carbon cycle through time. *Nat. Geosci.* **13**, 535–546 (2020).
45. Galvez, M. E. & Jaccard, S. L. Reducing capacity of rocks by high temperature chalcometric titration. *Chem. Geol.* 120016 (2020) doi:10.1016/j.chemgeo.2020.120016.
46. Augier, R. *et al.* Exhumation constraints for the lower Nevado-Filabride Complex (Betic Cordillera, SE Spain): a Raman thermometry and Tweequ multiequilibrium thermobarometry approach. *Bull. La Soc. Geol. Fr.* **176**, 403–416 (2005).
47. Connolly, J. A. D. Computation of phase equilibria by linear programming: A tool for geodynamic modeling and its application to subduction zone decarbonation. *Earth Planet. Sci. Lett.* **236**, 524–541 (2005).
48. Kuhn, B. K., Reusser, E., Powell, R. & Günther, D. Metamorphic evolution of calc-schists in the Central Alps, Switzerland. *Schweizerische Mineral. und Petrogr. Mitteilungen* **85**, 175–190 (2005).
49. Bebout, G. E. & Penniston-Dorland, S. C. Fluid and mass transfer at subduction interfaces—The field metamorphic record. *Lithos* **240**–**243**, 228–258 (2016).
50. Green, D. H., Hibberson, W. O., Kovacs, I. & Rosenthal, A. Water and its influence on the lithosphere-asthenosphere boundary. *Nature* **467**, (2010).
51. Bénard, A. *et al.* Oxidising agents in sub-arc mantle melts link slab devolatilisation and arc magmas. *Nat. Commun.* **9**, (2018).
52. Malaspina, N., Poli, S. & Fumagalli, P. The Oxidation State of Metasomatized Mantle Wedge: Insights

from C-O-H-bearing Garnet Peridotite. *J. Petrol.* **50**, 1533–1552 (2009).

53. Stolper, E. M., Shorttle, O., Antoshechkina, P. M. & Asimow, P. D. The effects of solid-solid phase equilibria on the oxygen fugacity of the upper mantle. *Am. Mineral.* **105**, 1445–1471 (2020).

54. Plank, T. & Langmuir, C. H. The chemical composition of subducting sediment and its consequences for the crust and mantle. *Chem. Geol.* **145**, 325–394 (1998).

Methods

Abundance of redox-sensitive elements. We extended a previous compilation[17] of ferric and ferrous iron contents in serpentinite from different geologic settings (n=758) (Fig.1a) to include alpine serpentinite from Malenco (N. Italy, n=42)[55,56] and 33 new analyses from CdA analysed by potentiometric titration. Bulk $Fe^{3+}/\Sigma Fe$ ratios are in excellent agreement with mineral mode estimates based on the measured amount of magnetite by saturation magnetization corrected for the paramagnetic fraction[16] and using the $Fe^{3+}/\Sigma Fe$ content of antigorite measured by XANES spectroscopy in selected samples[57]. Magnetite contents (Supplementary Fig. 2) comprise serpentinites from mid-ocean ridges (ODP Leg 153 MARK[18,58,59]), passive margins (ODP Leg 173 Iberia[58,59]), Puerto Rico Trench (NWPRT)[59], forearc (ODP Leg 125 Marianas[58,59]), alpine serpentinites[16,35,57], and prograde metaperidotite from CdA[4,35,57] and CdG[41]. Late-stage weathering of prograde metaperidotite may cause re-oxidation during hydration, therefore we only consider samples with < 4.5 wt.% H_2O for comparison with the thermodynamic predictions (Fig.1). Bulk carbon and sulphur contents are from this study and ref[2,11,36,41,60].

Computation of redox budget. The redox budget[61] is an extensive variable quantifying the ability of a rock–fluid system to potentially induce oxidation or reduction relative to an arbitrary reference redox state of interest. The specific redox budget (RB) is normalized to units of mol/kg and it is defined as,

$$RB = \sum_j n_j \cdot v_j$$

where v_j is the number of electrons required to take one mole of the element in the redox state *j* to the reference redox state, and n_j is the number of moles per kg of the element in the redox state *j* present in the system (rock and fluid). Here (Supplementary Table 1 and Fig. 3), we consider the redox budget of the solid rock as this is the only variable that can be measured after fluid extraction. For the whole mantle reference redox state[2], the oxidation state of iron, carbon and sulphur are Fe^{2+}, C^0 and S^{2-}, respectively, resulting in v_j of 1, -2, 4, 1 and 8 for Fe^{3+}, Fe^0, C^{4+}, S^- and S^{6+}. In the modelled system, the RB is computed based on the number of moles per kg of rock of the phases containing Fe^{3+}, Fe^0, C^{4+}, S^- or S^{6+} (hematite, native iron, magnesite, dolomite, calcite, pyrite, pyrrhotite, pyroxenes, garnet and anhydrite, Supplementary Fig. 3) multiplied by the number of redox-sensitive atoms in their structural formulae. For mineral phases having ferric iron in solid solution, the RB is weighted by the molar proportion of the ferric iron endmember (magnetite in spinel[62], $Fe_{0.875}S$ in pyrrhotite[9], magnesium ferri-tschermak's in orthopyroxene modified by J.A.D. Connolly from ref[63], and khoharite in garnet[64]) .

Phase equilibria. Phase equilibria and electrolyte fluid speciation were computed by Gibbs energy minimization using the PerpleX algorithm[65,66]. Forward thermodynamic modelling has been performed in the CFMACrSHCSO system using elements as thermodynamic system components (Ca–Fe–Mg–Al–Cr–Si–H_2–C–S_2–O_2) for metaserpentinite and metaperidotite and in the NKCFMASHCSO system

(Na–K–Ca–Fe–Mg–Al–Cr–Si–H_2–C–S_2–O_2) for the graphite-bearing metapelite[33,46] and GLOSS[54], as well as for the metasomatic infiltration models derived from them (bulk composition used are in Supplementary Table 1). Fluid saturation conditions were not imposed during the computation. Element components are preferred over oxide components when modelling electrolytic fluid speciation because C–O–H–S solvents in the fluid have a strong tendency to order for certain bulk compositions at low temperature[67]. Thermodynamic data for endmembers are taken from ref[68]. Considered solid solutions models were olivine (Ol), orthopyroxene (Opx), clinopyroxene (Cpx), chlorite (Chl), dolomite (Dol), magnesite (Mgs), epidote (Ep), staurolite (St), all of them from ref[69,70], pyrrhotite (Po)[68], amphibole (Amph(DHP))[71], garnet (Grt(WPH))[64], antigorite (Atg)[37], white mica (mica(CF))[72], biotite (Bi(WPH))[64], feldspar[73], Cr-bearing spinel (Mag)[62], talc (Tlc, ideal), brucite (B, ideal), anthophyllite (Anth, ideal), and pure endmembers hematite (hem), pyrite (py), anhydrite (anh), graphite (gr), quartz (q) and iron. We used models Chl(W)[74] and Cpx(HGP)[75] for graphite-bearing metapelite and GLOSS, whereas for the mantle wedge metasomatism modelling we used solid solution models specifically calibrated for the mantle[62]. The systems considered in our work allow the investigation of redox reactions among the Fe–C–S-bearing solid phases (pyrrhotite, pyrite, anhydrite, magnetite, hematite, iron, carbonates and graphite) and species (e.g. HS^-, SO_4^{2-}, $CaSO_{4(aq)}$ among many others) in an electrolyte aqueous C–O–H–S fluid. Non-modelled components (Ti, Mn and Ni) typically represent less than 0.5 wt.% (expressed as oxides) of the bulk rock composition. The absence of titanium and nickel prevents the modelling of phase assemblages containing ilmenite and pentlandite which typically occur in excess in high-pressure serpentinite and metaperidotites. The initial oxidation state of the redox-sensitive elements (Fe–C–S_2) is specified by the amount of O_2 in the system and requires a knowledge of the oxidation state of iron, carbon and sulphur (Supplementary, Table 1). However, the oxidation state of iron, carbon and sulphur are not imposed but are set by the stable phases obtained by Gibbs energy minimization (Supplementary Fig. 2 and 3). The geothermal gradient used to compute Fig. 2 and Supplementary Fig. 2-4) (P[bar] = –18057 + 37.9357 * T[K]) follows the P–T path inferred for CdA[76], and also applies for peak metamorphic conditions estimated for the CdG metaperidotite[41].

Solvent and speciation in the aqueous fluid. The neutrally charged solvent molecules considered in the fluid were H_2O–CO_2–CH_4–H_2–H_2S (thermodynamic data from ref.[68]) described by a generic hybrid fluid EoS with non-linear subdivision (COH-Fluid+ from ref[67]). The EoS for H_2O and CO_2 is PSEoS[77], whereas for other solvents is the MRK[78]. All other species are taken as solutes following the approach of ref.[67,79] (see Supplementary Table 2). Thermodynamic data for aqueous species are taken from the latest version of the DEW model[80]. The species $CO_{(aq)}$ and $SO_{2(aq)}$ are considered as solute species in the fluid, although they occur at very low concentrations (Supplementary Table 2). Organic species from the DEW model were excluded from the computation following ref[67]. The $Mg(SiO_2)(HCO_3)^+$ and $H_2CO_{3(aq)}$ species were also excluded as they were found to result in unrealistically high concentrations.

Back- and lagged-computation methods[67] give similar results at temperatures cooler than the complete serpentinite breakdown, but only the lagged method correctly models the complete loss of sulphur at higher temperatures because this method imposes mass balance conservation.

Infiltration models. The fluids in equilibrium with the graphite-bearing metapelite were first computed by Gibbs energy minimization at the P–T conditions of interest (650 ºC, 1.7 GPa, Supplementary Table 2) using MEEMUM from the PerpleX package[66] and the lagged calculation method[67]. This composition (renormalized to two hydrogen moles) was then equilibrated with the model serpentinite at the same P–T conditions at steps of 0.1 mol of fluid aliquot along 150 nodes (0-d infiltration mode), without fractionation of the fluid at each node. Additional computations fractionating the fluid at each node do not significantly modify the results. An example of the reequilibrated composition after interaction of 12 mol/kg with a fluid equilibrated with graphite-bearing metapelite is presented in the Supplementary Table 2. To model global subduction zones, the same procedure was repeated for all s 56 subduction zone segments at the P and T of the intersection of the antigorite breakdown with the slab surface based on the numerical model D80 from ref.[81] The intersection was found by solving the polynomial fitting of the antigorite dehydration curve from this study and the slab trajectories at the surface[81] as documented in ref.[82]. MEEMUM was then computed for the 56 P–T conditions for the two different fluid sources (graphite-bearing metapelite and GLOSS sediment) resulting in 112 different fluid compositions. Once these fluids were retrieved, 112 infiltration models were run with VERTEX at the specified P–T conditions. These computations generate multigrid outputs for all available properties accessible with WERAMI, including, mineral and fluid modes, dependent chemical potentials (used to compute $\Delta\log_{10}fO_2$[FMQ]) and the amount of solvents in the fluid (as mole fraction) and species concentration (as molalities, mol/kg). We provide a global dataset (source data) including $\Delta\log_{10}fO_2$[FMQ], bulk fluid composition and solvent-solute fluid composition for the intrinsic and the two sediment-infiltrated deserpentinisation models (using high and low reducing capacity fluids) for the 56 subduction transects and an extent of interaction of 12 mol/kg. A Python notebook is provided under request to generate the dataset for any desired extent of interaction.

Mantle wedge redox conditions. Two end-member bulk compositions were considered to compute the fO_2 of the mantle wedge before fluid infiltration (Fig. 3 and Supplementary Fig. 6): depleted MORB mantle source (DMM)[83] with a $Fe^{3+}/\Sigma Fe$ equal to 0.035, taken from the Primitive Upper Mantle, and adding S content of 119 μg/g;and a highly depleted mantle (sample PHN5239 from ref.[84]) with a $Fe^{3+}/\Sigma Fe$ equal to 0.021 and a 50 μg/g of S, taken as the lowest possible bound based on the Cu–S covariance in MORBs[85]. We chose fluids from the hottest and coldest subduction zones after 12 mol/kg interaction of the two fluids (graphite-bearing metapelite and GLOSS) with the reference serpentinite.

The aqueous fluid was fractionated at each node for mantle wedge infiltration models to reflect the low instantaneous fluid–rock ratio expected for pervasive fluid flow at mantle conditions.

Acknowledgements

This work is part of the project DESTINE (PID2019-105192GB-I00) funded by MICIN/AEI/10.13039/501100011033 and the FEDER program "una manera de hacer Europa". J.A.P.N. acknowledges a Ramón y Cajal contract (RYC2018-024363-I) funded by MICIN/AEI/10.13039/501100011033 and the FSE program "FSE invierte en tu futuro". This research is part of the Junta de Andalucia research group RNM-131.

Author contributions

J.A.P.N. conceived the project, processed the data, acquired funding and wrote the original manuscript. V.L.S-V. contributed to the conceptualization, performed the computations, organized the raw data and contributed to the writing of the manuscript. M.D.M. computed the global deserpentinisation conditions and assisted computations. M.T.G-P. contributed to the writing of the manuscript. C.J.G contributed to the conceptualization, acquired funding, t and writing of the manuscript.

References

55. Clément, M., Padrón-Navarta, J. A. & Tommasi, A. Interplay between Fluid Extraction Mechanisms and Antigorite Dehydration Reactions (Val Malenco, Italian Alps). *J. Petrol.* **60**, 1935–1962 (2019).
56. Lafay, R., Baumgartner, L. P., Putlitz, B. & Siron, G. Oxygen isotope disequilibrium during serpentinite dehydration. *Terra Nov.* **31**, 94–101 (2019).
57. Debret, B. *et al.* Evolution of Fe redox state in serpentine during subduction. *Earth Planet. Sci. Lett.* **400**, 206–218 (2014).
58. Klein, F. *et al.* Magnetite in seafloor serpentinite-Some like it hot. *Geology* **42**, 135–138 (2014).
59. Klein, F., Marschall, H. R., Bowring, S. A., Humphris, S. E. & Horning, G. Mid-ocean Ridge Serpentinite in the Puerto Rico Trench: from Seafloor Spreading to Subduction. *J. Petrol.* **58**, 1729–1754 (2017).
60. Paulick, H. *et al.* Geochemistry of abyssal peridotites (Mid-Atlantic Ridge, 15°20′N, ODP Leg 209): Implications for fluid/rock interaction in slow spreading environments. *Chem. Geol.* **234**, 179–210 (2006).
61. Evans, K. A. Redox decoupling and redox budgets: Conceptual tools for the study of earth systems. *Geology* **34**, 489–492 (2006).
62. Jennings, E. S. & Holland, T. J. B. B. A simple thermodynamic model for melting of peridotite in the system NCFMASOCr. *J. Petrol.* **56**, 869–892 (2015).
63. Holland, T. & Powell, R. Thermodynamics of order-disorder in minerals .2. Symmetric formalism applied to solid solutions. *Am. Mineral.* **81**, 1425–1437 (1996).
64. White, R. W., Powell, R. & Holland, T. J. B. Progress relating to calculation of partial melting equilibria

for metapelites. *J. Metamorph. Geol.* **25**, 511–527 (2007).
65. Connolly, J. A. D. Multivariable Phase-Diagrams - an Algorithm Based on Generalized Thermodynamics. *Am. J. Sci.* **290**, 666–718 (1990).
66. Connolly, J. A. D. The geodynamic equation of state: What and how. *Geochemistry, Geophys. Geosystems* **10**, (2009).
67. Connolly, J. A. D. & Galvez, M. E. Electrolytic fluid speciation by Gibbs energy minimization and implications for subduction zone mass transfer. *Earth Planet. Sci. Lett.* **501**, 90–102 (2018).
68. Holland, T. J. B. & Powell, R. An improved and extended internally consistent thermodynamic dataset for phases of petrological interest, involving a new equation of state for solids. *J. Metamorph. Geol.* no-no (2011) doi:10.1111/j.1525-1314.2010.00923.x.
69. Holland, T., Baker, J. & Powell, R. *Mixing properties and activity-composition relationships of chlorites in the system MgO-FeO-Al_2O_3-SiO_2-H2O*. vol. 10 http://pubs.geoscienceworld.org/eurjmin/article-pdf/10/3/395/4000281/395_gseurjmin_10_3_395_406_holland.pdf (1998).
70. Holland, T. J. B., Powell, R., Sciences, E. & Cb, C. An internally consistent thermodynamic data set for phases of petrological interest. *J. Metamorph. Geol.* **16**, 309–343 (1998).
71. Dale, J., Holland, T. & Powell, R. Hornblende-garnet-plagioclase thermobarometry: a natural assemblage calibration of the thermodynamics of hornblende. *Contrib. to Mineral. Petrol.* **V140**, 353–362 (2000).
72. Chatterjee, N. D. & Froese, E. A thermodynamic study of the pseudobinary join muscovite-paragonite in the system KAlSi3O8 - NaAlSi3O8 - Al2O3 - SiO2 - H2O. *Am. Mineral.* **60**, 985–993 (1975).
73. Fuhrman, M. L. & Lindsley, D. H. Ternary-Feldspar Modeling and Thermometry. *Am. Mineral.* **73**, 201–215 (1988).
74. White, R. W., Powell, R. & Johnson, T. E. The effect of Mn on mineral stability in metapelites revisited: New a-x relations for manganese-bearing minerals. *J. Metamorph. Geol.* **32**, 809–828 (2014).
75. Holland, T. J. B., Green, E. C. R. & Powell, R. Melting of Peridotites through to Granites: A Simple Thermodynamic Model in the System KNCFMASHTOCr. *J. Petrol.* **59**, 881–900 (2018).
76. Laborda-López, C. *et al.* High- P metamorphism of rodingites during serpentinite dehydration (Cerro del Almirez, Southern Spain): Implications for the redox state in subduction zones. *J. Metamorph. Geol.* **36**, 1141–1173 (2018).
77. Pitzer, K. S. & Sterner, S. M. Equations of state valid continuously from zero to extreme pressures with H2O and CO2 as examples. *Int. J. Thermophys.* **16**, 511–518 (1995).
78. Connolly, J. A. D. & Cesare, B. C-O-H-S fluid composition and oxygen fugacity in graphitic metapelites. *J. Metamorph. Geol.* **11**, 379–388 (1993).
79. Galvez, M. E., Connolly, J. A. D. & Manning, C. E. Implications for metal and volatile cycles from the pH of subduction zone fluids. *Nature* **539**, 420 (2016).
80. Huang, F. & Sverjensky, D. A. Extended Deep Earth Water Model for predicting major element mantle metasomatism. *Geochim. Cosmochim. Acta* **254**, 192–230 (2019).
81. Syracuse, E. M., van Keken, P. E. & Abers, G. A. The global range of subduction zone thermal models. *Phys. Earth Planet. Inter.* **183**, 73–90 (2010).

82. Menzel, M. D., Garrido, C. J. & López Sánchez-Vizcaíno, V. Fluid-mediated carbon release from serpentinite-hosted carbonates during dehydration of antigorite-serpentinite in subduction zones. *Earth Planet. Sci. Lett.* **531**, 115964 (2020).
83. Salters, V. J. M. & Stracke, A. Composition of the depleted mantle. *Geochemistry, Geophys. Geosystems* **5**, (2004).
84. Canil, D. *et al.* Ferric iron in peridotites and mantle oxidation states. *Earth Planet. Sci. Lett.* **123**, 205–220 (1994).
85. Ding, S. & Dasgupta, R. The fate of sulfide during decompression melting of peridotite – implications for sulfur inventory of the MORB-source depleted upper mantle. *Earth Planet. Sci. Lett.* **459**, 183–195 (2017).
86. Eberhard, L. Serpentinite phase relations - An experimental study on redox conditions and fluid migration in subduction zones. Bayreuth , 2021 . - VIII, 258 P. (Doctoral thesis, 2020 , University of Bayreuth, Faculty of Biology, Chemistry and Earth Sciences)
87. Cannaò, E. & Malaspina, N. From oceanic to continental subduction: Implications for the geochemical and redox evolution of the supra-subduction mantle. *Geosphere* **14**, 2311–2336 (2018).

Supplementary figures and tables

Figure 1. Global compilation of magnetite content in serpentinite and metaperidotite (Chl-harzburgite) against the water content (measured for CdA, this work and ref[36]) or loss of ignition (L.O.I.) as a proxy for water content for samples from the literature (see Methods). The observed decrease in magnetite content relative to common magnetite-bearing serpentinite is reproduced by deserpentinisation infiltrated with highly reducing fluids equilibrated with graphite-bearing metapelite. The decrease in magnetite for the intrinsic deserpentinisation model is coeval with the precipitation of hematite (dashed red line) which is not observed in natural samples.

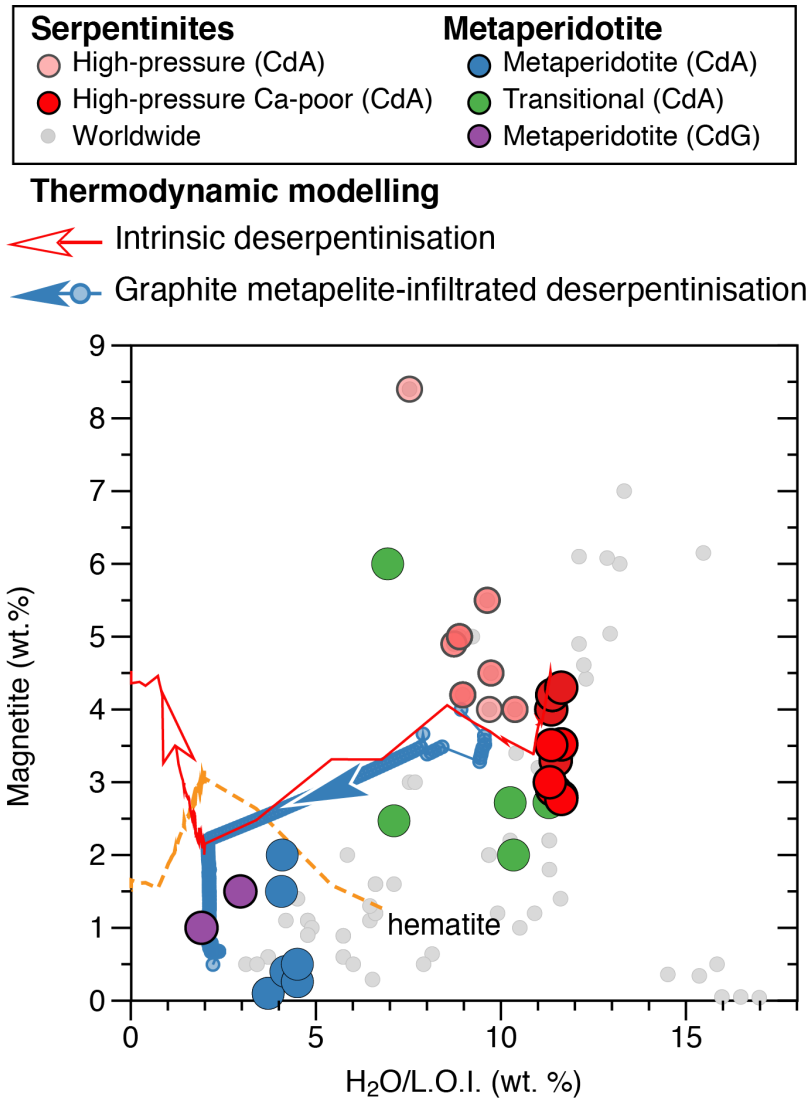

Figure 2. X(O_2)-P/T (along a thermal gradient, see Methods) pseudosection[10] for a representative Ca-poor serpentinite from CdA (sample Al98-05a[25]) with sulphur and carbon content from ref[36] (these values were confirmed by new, duplicate analyses) and ferric iron from this work (see Supplementary Table 1). The vertical line represents the intrinsic deserpentinisation for a fixed O_2 content of the system (Path I), corresponding to the bulk O_2 for sample Al98-05a (15.602 mol/kg is used instead of the measured 15.672 mol/kg for better agreement with the observed sequence of mineral assemblages at CdA; it likely reflects the amount of ferric iron in antigorite, not accounted for in the available solid solution models[86]). The horizontal path (IIa) shows schematically the evolution if the system is externally infiltrated by fluids equilibrated with metasedimentary rocks with a high reducing capacity (graphite-bearing metapelite). The quantitative evolution along path IIa is shown in Figure 2b in the main text (see also Supplementary Figure 5 for the evolution of the speciation in the fluid). The path IIb corresponds to the prograde evolution after the graphite metapelite-infiltrated deserpentinisation potentially followed by CdG.

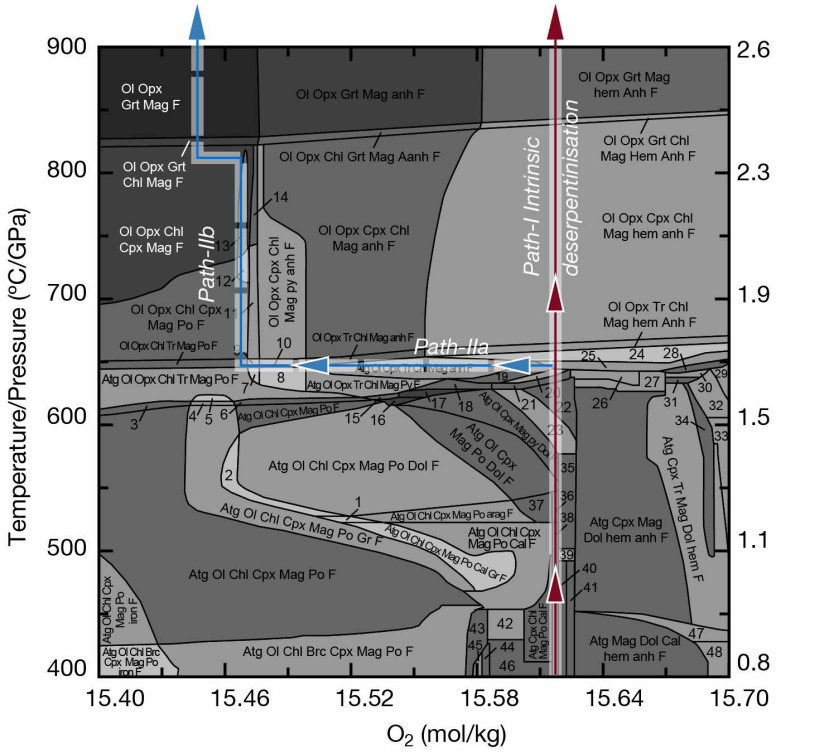

Numbered fields

1 Atg Ol Chl Cpx Mag Po arag F
2 Atg Ol Chl Cpx Mag Po Dol F
3 Atg Ol Chl Tr Mag Po F
4 Atg Ol Chl Tr Mag Po Gr F
5 Atg Ol Opx Chl Tr Mag Po Gr F
6 Atg Ol Chl Tr Mag Po F
7 Atg Ol Opx Chl Tr Mag Po Py F
8 Atg Ol Opx Chl Tr Mag Py Anh F
9 Ol Opx Chl Tr Mag Po Py F
10 Ol Opx Chl Tr Mag Py Anh F
11 Ol Opx Chl Cpx Mag Po Py F
12 Ol Opx Chl Cpx Mag Po Gr F
13 Ol Opx Chl Cpx Mag Gr F
14 Ol Opx Chl Cpx Mag Py F
15 Atg Ol Tr Chl Mag Py F
16 Atg Ol Cpx Mag Py F
17 Atg Ol Tr Mag Py F
18 Atg Ol Opx Tr Mag Py F
19 Atg Ol Opx Tr Mag Anh F
20 Atg Ol Opx Tr Mag Mgs Anh F
21 Atg Ol Tr Mag Mgs Anh F
22 Atg Ol Cpx Mag Anh Dol F
23 Atg Ol Cpx Mag Py Anh Dol F
24 Atg Ol Opx Tr Chl Mag Hem Anh F
25 Atg Ol Opx Tr Mag Hem Anh F
26 Atg Ol Tr Mag Mgs Hem Anh F
27 Atg Ol Cpx Mag Dol Hem Anh F
28 Atg Opx Tr Mag Hem Anh F
29 Atg Tr Tlc Mag Mgs Hem Anh F
30 Atg Ol Opx Tr Mag Mgs Hem F
31 Atg Ol Tr Mag Mgs Hem F
32 Atg Tr Mag Dol Hem Cal Anh F
33 Atg Tr Tlc Mag Dol Hem Anh F
34 Atg Tr Mag Dol Hem Anh F
35 Atg Cpx Mag Py Dol Anh F
36 Atg Cpx Mag Po Py arag F
37 Atg Ol Cpx Mag Po arag F
38 Atg Cpx Mag Po Py Cal F
39 Atg Cpx Mag Py Dol Cal Anh F
40 Atg Cpx Mag Py Cal Anh F
41 Atg Mag Py Dol Cal Anh F
42 Atg Chl Brc Cpx Mag Po Cal F
43 Atg Chl Brc Cpx Mag Po F
44 Atg Chl Brc Mag Po Gr F
45 Atg Chl Brc Cpx Mag Po Gr F
46 Atg Chl Mag Po Cal Gr F
47 Atg Cpx Mag Dol Cal Hem Anh F
48 Atg Tr Mag Dol Cal Hem Anh F

Figure 3. Absolute concentration of oxygen-sensitive components in the solids (expressed as mol/kg of rock Al98-05a) for the pseudosection shown in Supplementary Figure 2 (see also Figure 2 in the main text for the contouring of oxygen fugacity relative to the buffer FMQ). All panels were computed from the absolute amounts of mineral phases containing oxygen-sensitive components and their concentration in pure and solid solution endmembers from WERAMI outputs. Computations used the back-calculated method for fluid speciation in PerpleX, except for pannel S^{6+} that was computed using the lagged speciation method that allows mass balance constrains in the region below the complete serpentinite dehydration. The last panel shows the redox budget referred to the whole mantle reference redox state (Methods).

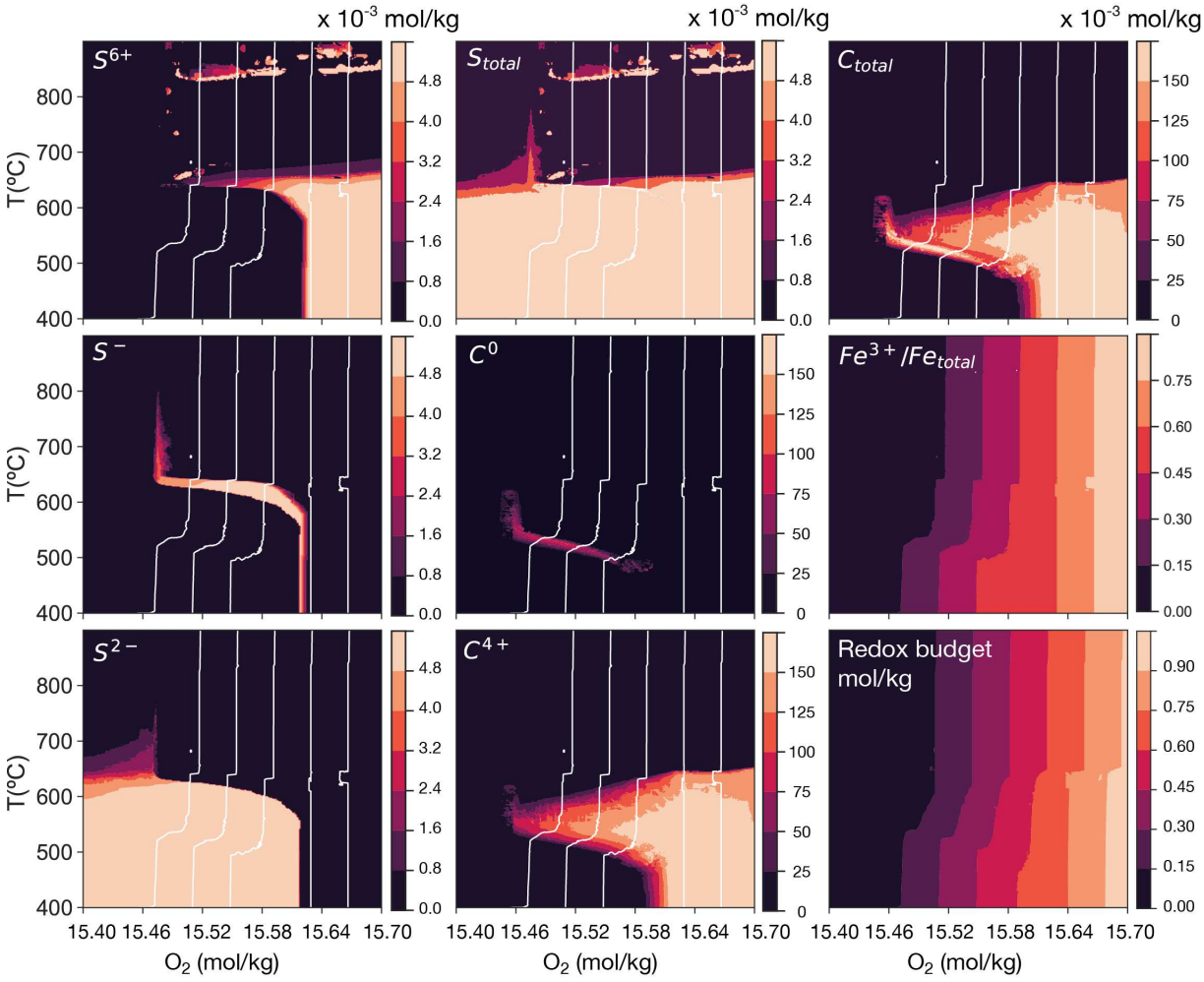

Figure 4. Evolution of key parameters along intrinsic deserpentinisation (intrinsic path I in Figure 2, red vertical line). (a) X_{Mg} in antigorite and their dehydrated product olivine and orthopyroxene; (b) H_2O content hosted in the solid phases; (c) and (d) bulk sulphur and carbon contents retained in the solid phases; (e) evolution of the oxygen fugacity relative to the FMQ buffer. The blue region corresponds to the temperature conditions of dehydration in Cerro del Almirez (CdA). Note that none of the observables (X_{Mg}, S and C content, see Fig. 2b in the main text) agrees with the model predictions along with the intrinsic deserpentinisation model.

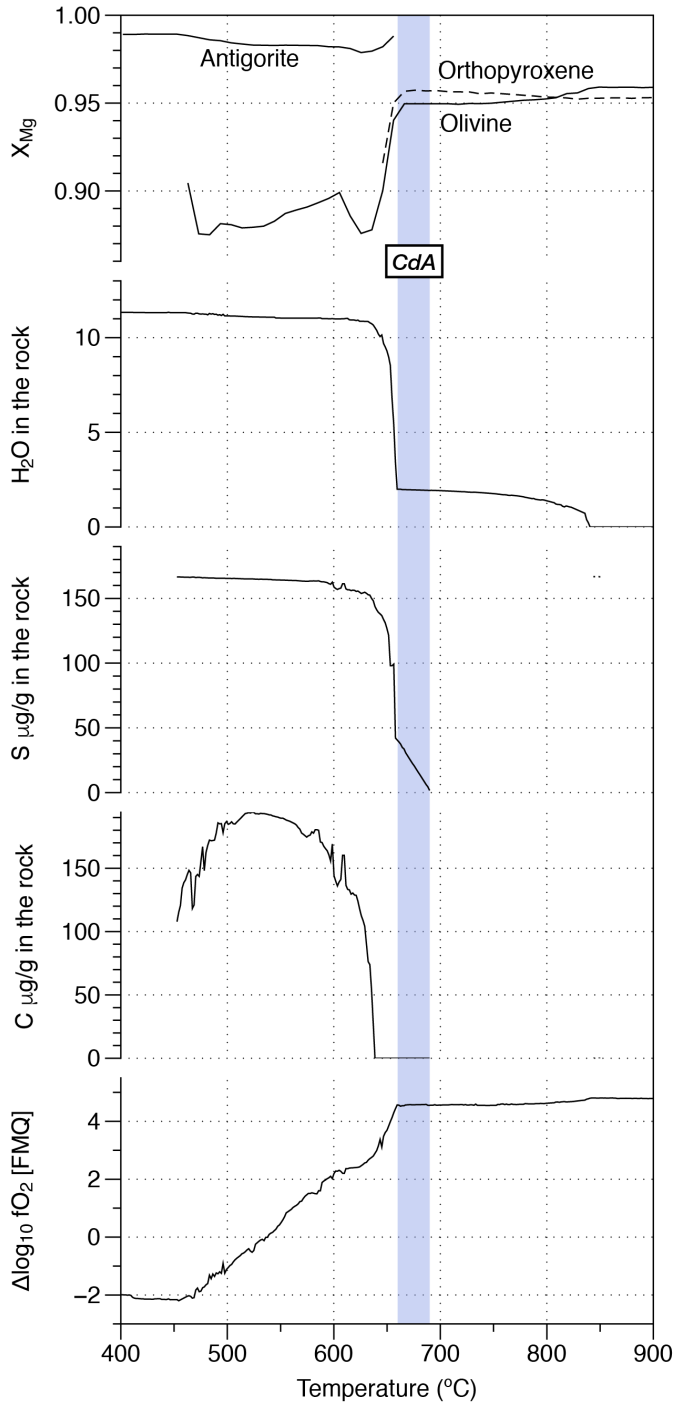

Figure 5. a. Fluid speciation evolution during the infiltration of a partially dehydrated serpentinite with a fluid equilibrated with a graphite-bearing metapelite at 650 ºC and 1.7 GPa. The solvent species H_2S and CO_2 are expressed as mole fraction, whereas the solute species are expressed as molality (mol/kg). The main oxidising species (HSO_4^-) is represented on a linear scale whereas other less abundant species are on a logarithmic scale. b. Modal (vol.%) pyrite abundance in the metaperidotite induced by graphite metapelite fluid infiltration.

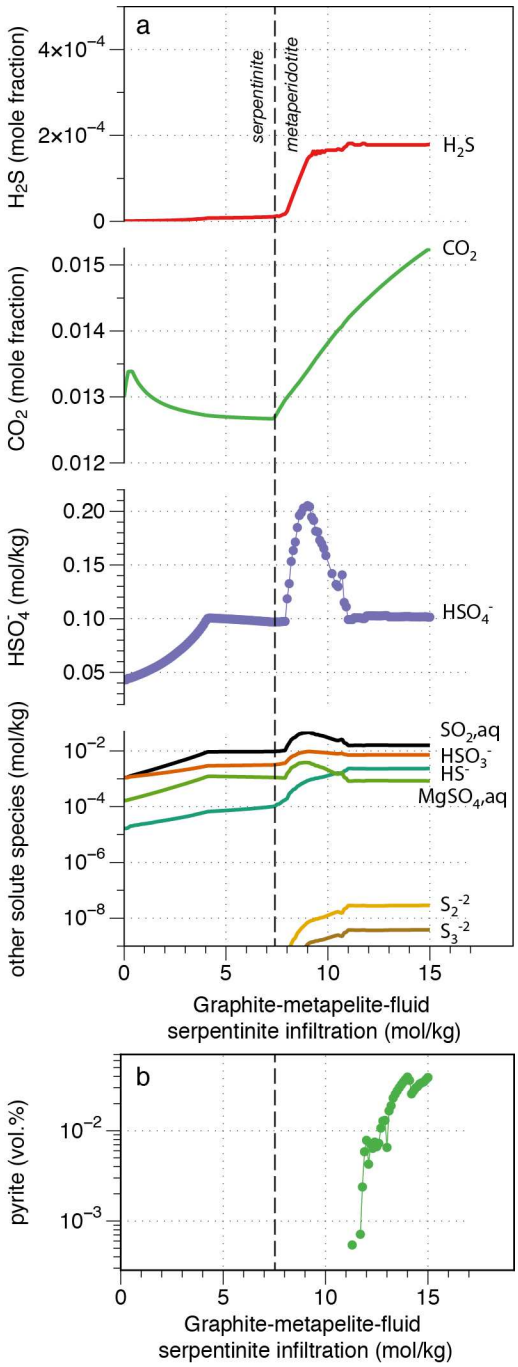

Figure 6. Intrinsic deserpentinization oxygen fugacity conditions (a) relative to the FMQ buffer, $\Delta\log_{10}fO_2$[FMQ] and in absolute values (b) for a representative metaserpentinite (sample Al98-05a, see Supplementary, Table 1) in a pressure-temperature space. Yellow dots are pressure-temperature deserpentinisation conditions at the slab surface for a worldwide compilation of subduction zones[81,82], geographically located in (c), (d) Difference between the slab surface intrinsic deserpentinisation and the mantle wedge oxygen fugacity (expressed as $\Delta\log_{10}fO_2$[FMQ]) along the 1000ºC isotherm.

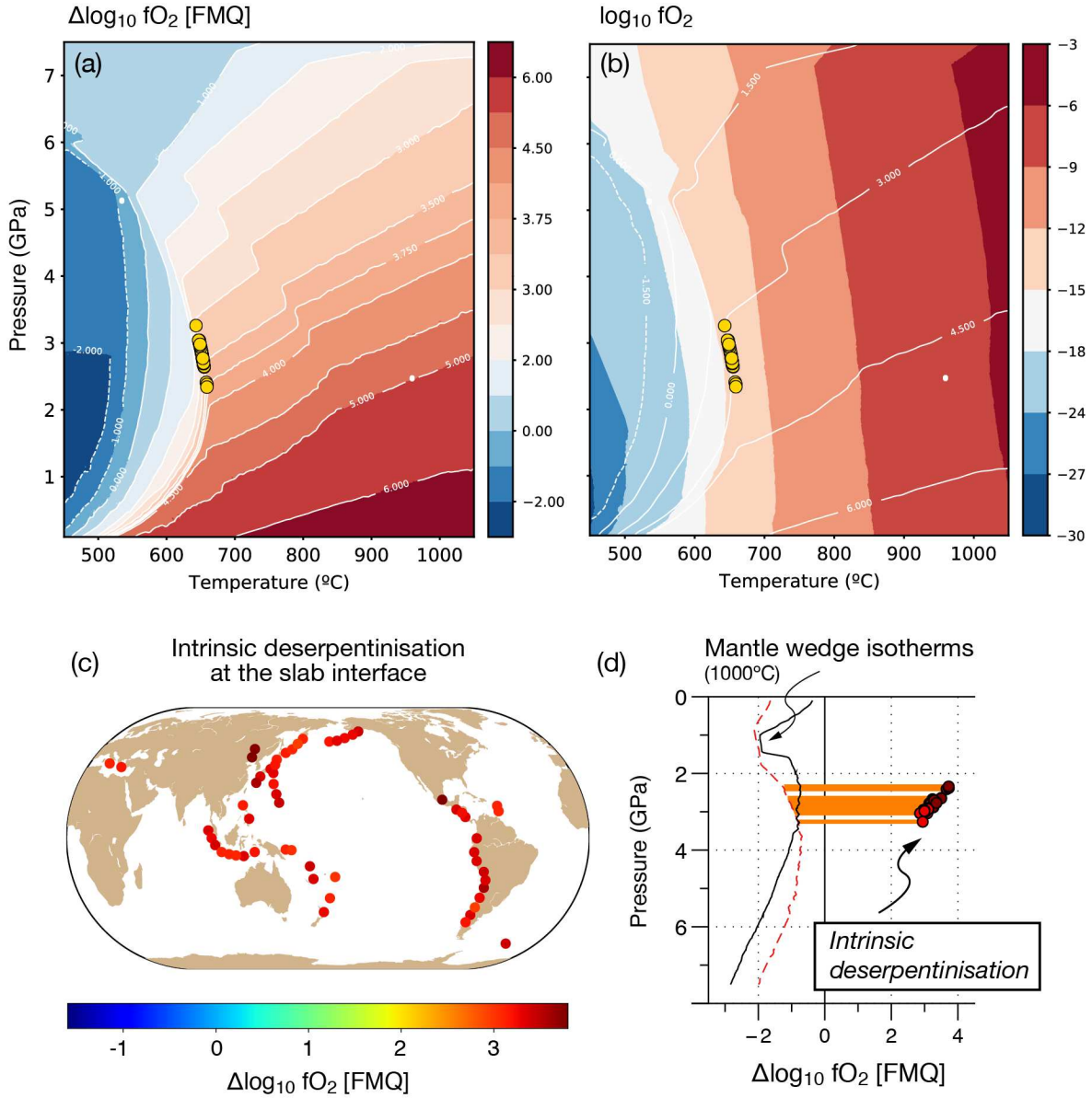

Figure 7. Effect of peridotite mantle wedge depletion on the $\Delta\log_{10}fO_2$[FMQ] evolution during fluxing by different types of deserpentinisation slab fluids. The left panel shows the results for (a) a depleted MORB mantle wedge source[83] (DMM) and (b) an ultradepleted mantle wedge source[84], both for a hot (Central Cascadia) and a cold (Tonga) subduction zone. The mantle wedge $\Delta\log_{10}fO_2$[FMQ] evolution of the mantle wedge fluxed by fluids sourced from intrinsic deserpentinisation and sediment-infiltrated deserpentinisation fluids produced by the infiltration of 12 mol/kg of fluids equilibrated with GLOSS and graphite-bearing metapelite. Right panels are the contours of the initial $\Delta\log_{10}fO_2$[FMQ] of the mantle wedge for a DMM (upper panel) and ultradepleted source (lower panel) before fluxing with slab fluids; shown as yellow dots are the initial $\Delta\log_{10}fO_2$[FMQ] conditions at the 1000 ºC of the mantle wedge for a worldwide compilation of dehydration conditions in hot to cold subduction zones. Central Cascadia (hot subduction) and Tonga (cold subduction) correspond, respectively, to a minimum (2.4 GPa) and maximum pressure (3.3 GPa) for the dehydration of serpentinisation at the slab surface. Note that the initial $\Delta\log_{10}fO_2$[FMQ] conditions depend on the thermal regime of the subduction zone and the depletion of the mantle wedge source, but have a subsidiary effect on the $\Delta\log_{10}fO_2$[FMQ] evolution of the mantle wedge during fluxing of different types of deserpentinisation fluids.

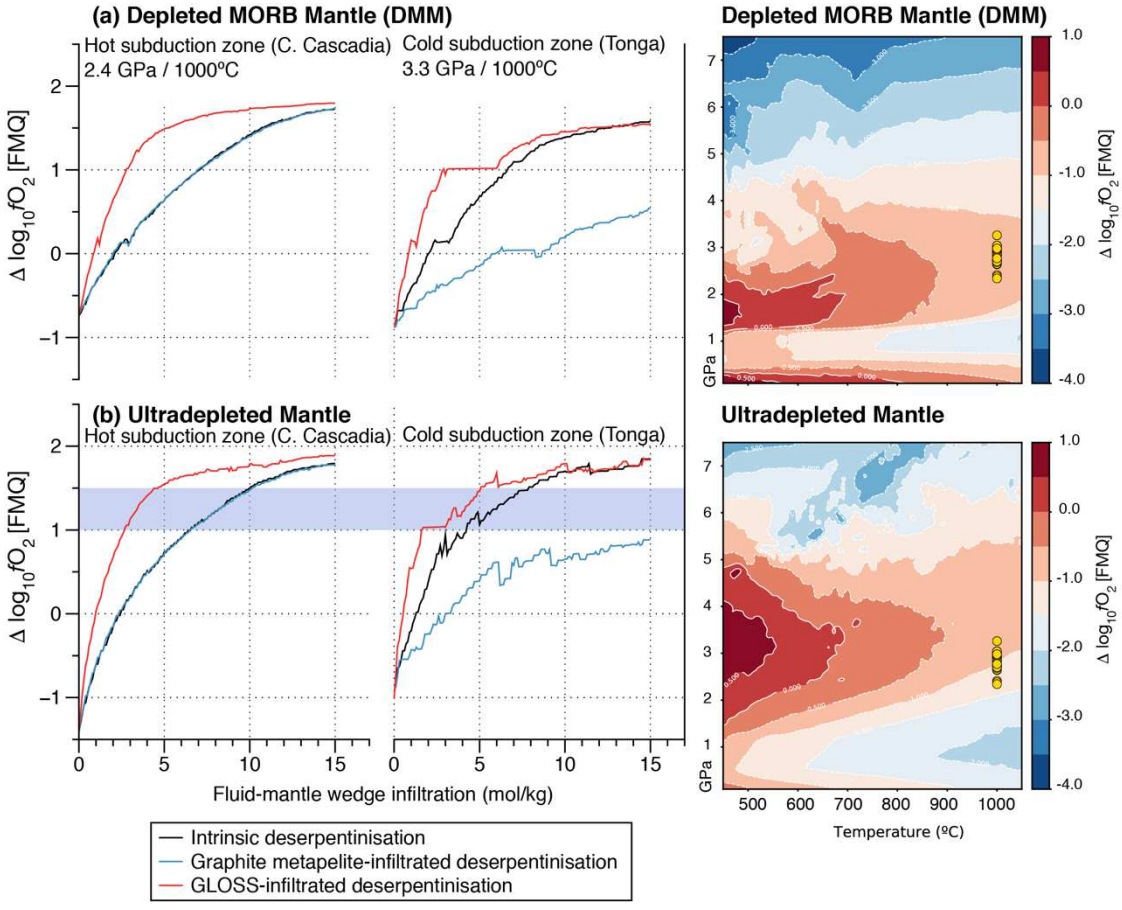

Figure 8. (a) Evolution of the $\Delta\log_{10}fO_2$[FMQ] and the concentration of HSO_4^- —relative to the intrinsic deserpentinisation fluid (ID)— during infiltration of fluids equilibrated with metasedimentary rocks with a high reducing capacity (graphite-bearing metapelite) for a worldwide compilation of subduction zones[81,82] (colour-coded for the pressure at which the serpentinite dehydrates at the slab surface, Source Data). (b) The capacity of these modified, serpentinite-derived fluids (empty dots in a) to oxidise the mantle wedge on top of the slab at near wet-solidus conditions is computed for the hottest (Central Cascadia) and coldest (Tonga) subduction zones. A minimum value range of $\Delta\log_{10}fO_2$[FMQ] inferred for oxidised IAB source and recorded by high-pressure metasomatized mantle atop of the slab[52,8752,87] is given as a horizontal blue-shaded range. Sediment (graphite-bearing)-serpentinite derived fluids have a variable capacity to oxidise the mantle wedge for hot and cold subduction zones, a variable potential that is directly related to the contrasting solubility of HSO_4^- for the two extreme thermal cases. The metasomatized mantle wedge has an initially depleted composition[83]. Squares and stars on the red and blue lines indicate the condition range limits at which pyrrhotite (Po), or anhydrite (anh) are the stable minerals hosting S in the rocks. For an ultradepleted MORB mantle, see Supplementary, Fig. 7. For interaction with sediments with low reducing capacity (GLOSS), see Fig. 3 in the main text.

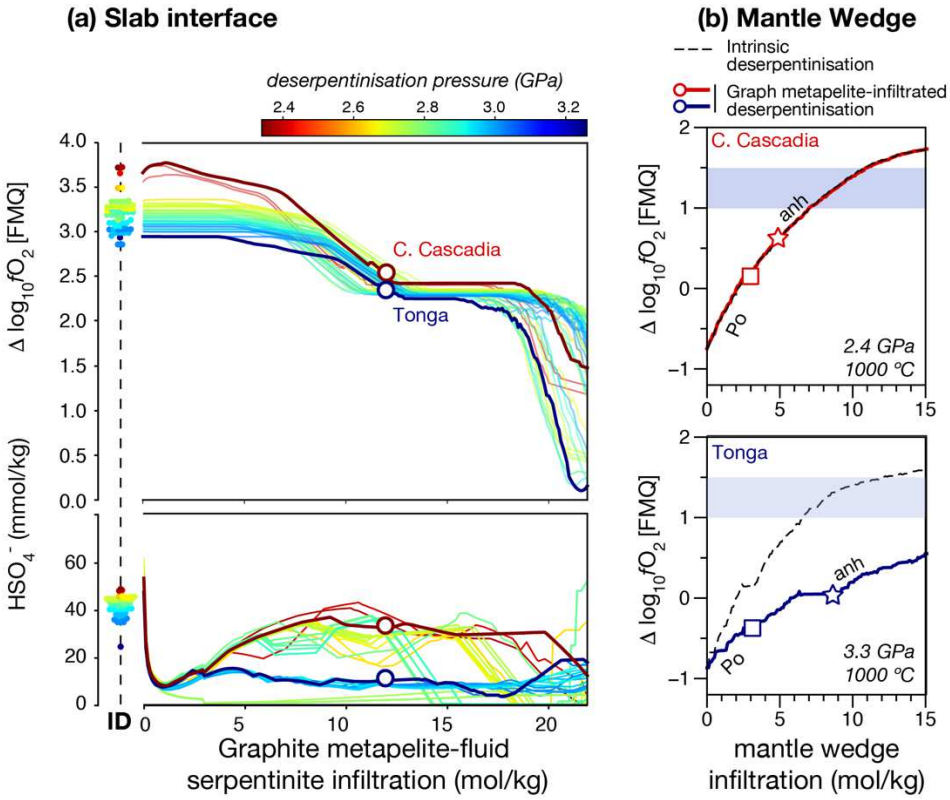

Supplementary Tables

Supplementary Table 1. Bulk rock compositions used for thermodynamic modelling.

Supplementary Table 2. Fluid composition and speciation for CdA peak metamorphic conditions at intrinsic dehydration and after interaction (12 mol/kg) with sediment with high reducing capacity

Source data

Supplementary file (csv). Worldwide subduction zone database[81] used to compute the pressure and temperature conditions for the slab surface deserpentinisation[82]. These pressure and temperature conditions are used to compute the intrinsic fluid chemistry and the fluid composition for high and low-reducing capacity sediments (graphite and GLOSS respectively) that are used for infiltration at the same serpentinite dehydration pressure and temperature conditions. Main species are given for the three cases: intrinsic (_intr) and for infiltration of 12 mol/kg for the cases of graphite-bearing and GLOSS sediments derived fluids (_graph and _gloss). Fluid bulk compositions are given in mol per formula unit of fluid and species concentrations are given in mol/kg. This database can be generated for other degrees of infiltration using a Jupyter notebook available upon request.

Supplementary Files

This is a list of supplementary files associated with this preprint. Click to download.

- ExtendedDataTable2.pdf
- ExtendedDataTable1.pdf
- ExtendedDataFigure1.pdf
- ExtendedDataFigure2.pdf
- ExtendedDataFigure3.pdf
- ExtendedDataFigure4.pdf
- ExtendedDataFigure5.pdf
- ExtendedDataFigure6.pdf
- ExtendedDataFigure7.pdf
- ExtendedDataFigure8.pdf